Journal of
Synchrotron
Radiation

ISSN 0909-0495

Received 21 October 2005
Accepted 9 March 2006

Evaluation of imaging performance of a taper optics CCD 'FReLoN' camera designed for medical imaging

Paola Coan,[a] Angela Peterzol,[b] Stefan Fiedler,[a,c] Cyril Ponchut,[a] Jean Claude Labiche[a] and Alberto Bravin[a]*

[a]European Synchrotron Radiation Facility, BP 220, 6 rue Horowitz, 38043 Grenoble CEDEX 9, France, [b]Dipartimento di Fisica, Università di Trieste e INFN, Sezione di Trieste, via Valerio 2, 34100 Trieste, Italy, and [c]EMBL, Notkestrasse 85, Building 25a, D-22603 Hamburg, Germany. E-mail: bravin@esrf.fr

The purpose of this work was to assess the imaging performance of an indirect conversion detector (taper optics CCD 'FReLoN' camera) in terms of the modulation transfer function (MTF), normalized noise power spectrum (NNPS) and detective quantum efficiency (DQE). Measurements were made with a synchrotron radiation laminar beam at various monochromatic energies in the 20–51.5 keV range for a gadolinium-based fluorescent screen varying in thickness; data acquisition and analysis were made by adapting to this beam geometry protocols used for conventional cone beams. The presampled MTFs of the systems were measured using an edge method. The NNPS of the systems were determined for a range of exposure levels by two-dimensional Fourier analysis of uniformly exposed radiographs. The DQEs were assessed from the measured MTF, NNPS, exposure and incoming number of photons. The MTF, for a given screen, was found to be almost energy independent and, for a given energy, higher for the thinnest screen. At 33 keV and for the 40 (100) μm screen, at 10% the MTF is 9.2 (8.6) line-pairs mm^{-1}. The NNPS was found to be different in the two analyzed directions in relation to frequency. Highest DQE values were found for the combination 100 μm and 25 keV (0.5); it was still equal to 0.4 at 51.5 keV (above the gadolinium *K*-edge). The DQE is limited by the phosphor screen conversion yield and by the CCD efficiency. At the end of the manuscript the results of the FReLoN characterization and those from a selected number of detectors presented in the literature are compared.

© 2006 International Union of Crystallography
Printed in Great Britain – all rights reserved

Keywords: medical imaging; image detectors; image quality.

1. Introduction

Over the past ten years synchrotron radiation has become a paradigmatic X-ray radiation source for preclinical and clinical X-ray imaging medical research. Several characteristics of synchrotron radiation sources are highly interesting for medical applications. The energy of quasi-monochromatic beams, delivered by X-ray monochromators, can be chosen over a wide energy range and can be optimized with sample characteristics; in this way an efficient use of the radiation and a minimization of the delivered dose can be simultaneously achieved (Suortti & Thomlinson, 2003; Arfelli *et al.*, 2000). Quasi-monochromatic beams also permit the complete removal of beam hardening artefacts (Tafforeau *et al.*, 2006) and the application of *K*-edge subtraction techniques, by injecting a contrast agent and temporally subtracting the two images (Bertrand *et al.*, 2005; Monfraix *et al.*, 2005; Adam *et al.*, 2005). The small source size (~20–200 μm in the vertical direction) and large source–sample distances (30–200 m in most of the synchrotron radiation beamlines) determine penumbras on the micrometric scale, and therefore the spatial resolution, in most of the cases, is limited only by the detector characteristics (Follet *et al.*, 2005). The minimal penumbra effect in combination with the small vertical divergence of the beam allows imaging with the detector placed at many meters from the object; images therefore appear almost scatter-free. In addition, when beamline optics conserves the transverse coherence of the beam, the phase-contrast imaging techniques can be applied (Pagot *et al.*, 2005; Coan *et al.*, 2005).

The presently developed synchrotron radiation imaging techniques require a detector of sufficient field of view for

small animal imaging (~10 cm), with a pixel size suitable for high-resolution imaging (50 μm or smaller). *In vivo* projection and tomographic studies require a low-noise and fast-readout system adapted to a laminar beam. In addition, the detector must maintain a high efficiency over a wide energy range, to minimize the dose delivered to the sample and to minimize the imaging time.

Large area detectors specifically developed for synchrotron radiation imaging and suitable for medical applications are extremely rare [to our best knowledge (Yagi, Inoue & Oka, 2004; Yagi, Yamamoto *et al.*, 2004)]. However, several commercial detectors for X-ray medical imaging exist on the market, highlighting simultaneously one or several of such characteristics, but unfortunately do not feature all at the same time.

Literature on medical radiology has mainly focused on amorphous selenium (a-Se) or amorphous silicon (a-Si) flat-panel (FP) and charge-coupled device (CCD) detectors coupled to different kinds of scintillators. In most of the cases detectors with a large field of view are generally characterized by rather large pixel sizes (~0.1–0.2 mm) (Granfors & Aufrichtig, 2000; Samei, 2003; Samei & Flynn, 2003). Higher spatial resolutions and good performances in terms of detective quantum efficiency (although strongly energy-dependent) are offered by a-Se and a-Si FPs coupled to gadolinium oxysulphide (GOS) screens, and by CCDs coupled to thallium-doped caesium iodide (CsI:Tl) screens (Goertzen *et al.*, 2004). Nevertheless, the field of view and/or the readout speed do not always fit the specific needs of the different medical imaging applications performed at synchrotron radiation facilities.

A more detailed discussion on detectors presented in the literature is reported in §5.

To match the specific requirements of synchrotron radiation medical imaging, the European Synchrotron Radiation Facility (ESRF) has developed a taper optics CCD fast-readout low-noise 'FReLoN' detector, whose evaluation is presented here. The FReLoN camera is characterized by a specific optics, which has been tailored for medical imaging purposes. The electronics and the data acquisition system, also developed at the ESRF, have been incorporated in several cameras (>10) used at different ESRF beamlines, each one coupled to a beamline-tailored optics.

The large-area transfer characteristic, the modulation transfer function, the noise power spectrum and the detective quantum efficiency have been calculated at different beam energies and for two different X-ray converters (fluorescent screens).

Unlike conventional sources, there is no established standard procedure for a complete evaluation of the detector performances when a laminar X-ray beam is used; neither is there, to our best knowledge, any reference in the literature on this subject.

In this paper we present in detail how we have adapted to this case the image quality assessment procedures used for conventional sources.

2. Materials and methods

2.1. The ID17 biomedical beamline at the ESRF

The detector has been characterized at the ID17 biomedical beamline of the ESRF; the X-ray source is a 21-pole variable-field wiggler (B_{max} = 1.6 T) of the ESRF 6 GeV electron machine. The photon source size is 125 μm (H) × 25 μm (V), expressed as full width at half-maximum (FWHM), which produces a high intense continuous spectrum of X-rays up to several hundreds of keV. The synchrotron radiation beam dimensions at the experimental station, which is located at 150 m from the source, are about 150 mm (H) × 10 mm (V).

Before entering the experimental station the X-ray beam is monochromated by a fixed-exit Si(111) double bent Laue crystal; this device can deliver quasi-monochromatic X-ray beams ($\Delta E/E \simeq 0.2\%$) in the energy range 20–90 keV (Suortti *et al.*, 2000). A set of remotely controlled horizontal and vertical slits allows the precision and reproducibility of the beam dimensions to be defined down to 5 μm. The monochromatic beam intensity can be controlled *via* a set of plexiglas attenuators positioned just after the monochromator. Finally, a remote-controlled shutter system separates the monochromator hutch from the experimental hutch where samples (at 145–152 m from the source) and detectors (at 152 m from the source) are installed.

2.2. The 'FReLoN' camera detector

The detector system we present in this work is a fast-readout low-noise (FReLoN) CCD camera coupled to a fiberoptical taper. This detector has been developed at the ESRF for a broad range of applications; its specifications were initially tailored for computed tomography applications in diffraction enhanced imaging mammography (Bravin *et al.*, 2003).

The FReLoN taper optics shows an active input surface of 94 mm × 94 mm where X-rays are converted to visible light by a fluorescent screen; this secondary radiation is then guided by a fiberoptic taper with a 3.2:1 reduction ratio and extra-mural absorption (Schott) onto the 2048 pixel × 2048 pixel 14 μm × 14 μm CCD (Atmel, USA). This reduction allows an effective pixel size of about 46 μm × 46 μm to be achieved.

Thanks to a careful design of the electronics and to a Peltier-type cooling of the CCD (standard operation at 255 K), both readout and dark signal levels are kept low (1.4 ADU pixel^{-1} r.m.s.[1] and 0.01 ADU pixel^{-1} s^{-1} r.m.s. without binning, respectively). At the same time a maximum readout speed of 20 Mpixels s^{-1} through four outputs provides the possibility of high-frame-rate imaging (4.2 frames s^{-1}) in full-size image mode without binning (Fig. 1). The gain is constant and it is 18 electrons ADU^{-1}; the maximum analogical-to-digital readout of 2^{14} bits corresponds to 3×10^4 electrons whatever the binning applied.

The fluorescent screen can be easily exchanged in order to optimize the X-ray conversion with the different experimental applications and the selected energy. In this work we report

[1] Analogical-to-digital unit (ADU) and root mean square (r.m.s.).

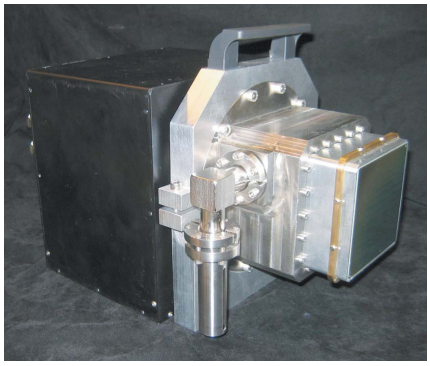

Figure 1
The taper optics FReLoN camera.

the results of the characterization of the camera coupled to powder phosphor screens (Gd2O2S:Tb, 5 g cm^{-3} density) of 40 µm and 100 µm thicknesses. The thin screen favors the spatial resolution at the expense of absorption efficiency, whereas the thicker screen provides the opposite compromise. Both screens consist of an active phosphor layer deposited on a thin plastic film substrate, the active layer being in direct contact with the fiberoptic taper input surface.

Taking into account the phosphor screen light yield, the optical coupling efficiency and the CCD quantum efficiency, the system quantum conversion ratio with the 40 µm screen is 12–14 electrons per absorbed 20 keV photon.

2.3. The 'FReLoN' camera readout system

The camera offers a set of acquisition/readout modes adapted to various experimental conditions. The CCD lines can be read independently or binned either horizontally and vertically.

In the so-called 'full frame mode', used for projection imaging, the sample must be scanned through the fan beam while the detector is moved in the same direction. At the end of the scan the whole CCD is electronically split into four quadrants, each read out by a channel at 206 µs per line (Fig. 2). Small regions of interests (ROIs) can also be selected and, if this is the case, the readout time is proportionally reduced.

The 'pipeline mode' is used for computed tomography imaging. The sample is scanned in front of the detector, which is kept stationary: the same lines are thus continuously exposed (their number depends on the beam height on the camera). The image is performed by illuminating $n_{\rm lin}$ lines at $n_{\rm dist}$ pixels from the nearest output channel. Each part of the image is then shifted towards the closest serial outputs (10 µs per line) where each line is read out (206 µs per line) (Fig. 3).

The total dead time is given by

$$\text{Dead time} = (n_{\rm dist} + n_{\rm lin})10\,\mu\text{s} + (n_{\rm lin}/\text{bin})\,206\,\mu\text{s}, \quad (1)$$

where bin corresponds to the chosen binning factor.

The number of lines that can be recorded in this mode is limited only by the RAM memory of the acquisition computer.

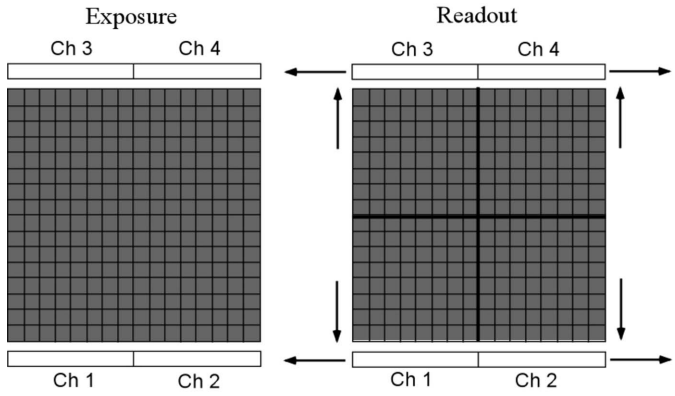

Figure 2
Full frame mode. Readout starts at the end of the exposure; each of the four quadrants (1024 pixel × 1024 pixel) is read out by a channel.

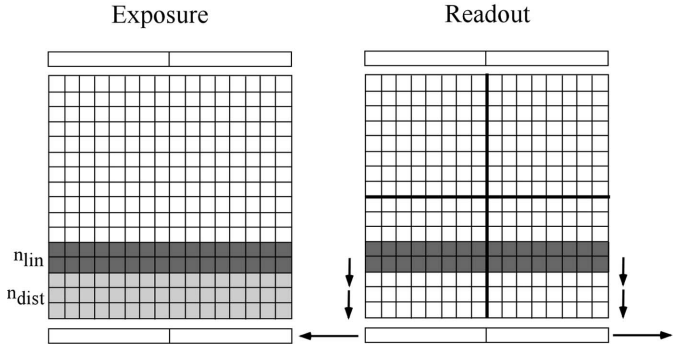

Figure 3
Pipeline mode. The image size is reduced to $n_{\rm lin}$ lines at $n_{\rm dist}$ (in the figure, $n_{\rm lin} = 2$ and $n_{\rm dist} = 3$) from the nearest output channels. This image is then sequentially treated as in the full frame mode, but only two channels on one side of the CCD are used for the readout.

A variation of the 'pipeline' mode (called 'concatenate mode') consists of the readout of a ROI between two movements of the sample without moving the detector; the image is then reconstructed as the pile-up of the different ROIs. This last variant has been used for the acquisition of the edge profiles (edge spread function) for the calculation of the modulation transfer function.

The maximum possible binning for these modes is 2 lines (H) × 2 lines (V) for the 'full frame mode', and 2 lines (H) × 1024 lines (V) for the 'pipeline' and the 'concatenate' modes.

A further acquisition mode, the so-called 'hybrid mode', has been implemented for faster computed tomography imaging. As in the pipeline mode, the detector is stationary and each projection is made of a few lines ($n_{\rm lin}$). After being illuminated, the lines are shifted towards the two farthest outputs, to fill the CCD. This new 'image', made of elementary parts, is then read out as in the full frame mode (Fig. 4). This procedure reduces the dead time between two projections but their maximum number is limited to $2048/n_{\rm lin}$.

2.4. The reference detector: the germanium pixel detector

Measurements of the detector exposure were performed by using a high-purity germanium detector operating at the

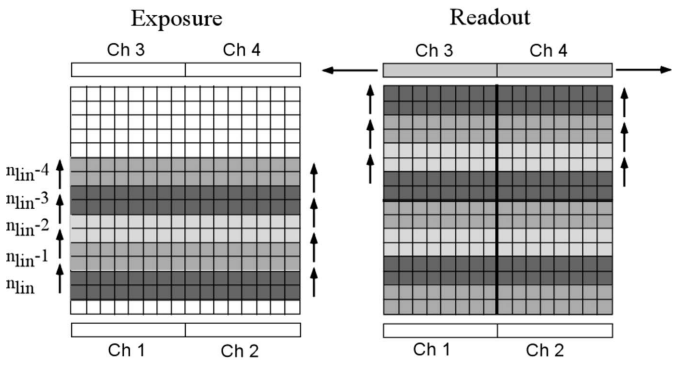

Figure 4
Hybrid mode. The full frame is filled by elementary 'pipeline mode' images; then the readout of the CCD is performed.

liquid-nitrogen temperature. It is made from a monolithic P-type Ge crystal, 2 mm thick, 160 mm long, 10 mm high and electrically segmented into two rows of 432 parallel strips each (0.35 mm pitch). It is protected by a 0.5 mm-thick beryllium window (Elleaume *et al.*, 1999). The 16-bit electronics works in charge integration mode. It allows a highly efficient detection (Peterzol *et al.*, 2003) of X-rays in the energy range used for the characterization of the FReLoN camera. The germanium detector and the FReLoN camera are installed on top of each other on the same remotely controlled support that can vertically translate; in this way, the two detectors can be alternatively positioned in the beam, allowing a constant distance from the source.

2.5. Large-area transfer characteristic

The linearity of the digital system has been verified in the exposure range used for the noise power spectrum measurements. The verification of the system linearity response is necessary to allow for the direct use of the digital pixel value in the rest of the analysis; in this way the linear system approach can be applied to characterize the detector performances in the spatial-frequency domain (Cunningham, 2000). A large-area transfer characteristic curve has been determined by measuring the detector output in terms of pixel values *versus* the input photon fluency. In the noise power spectrum study, ten flat-field images per energy and per exposure level have been acquired in pipeline mode. For each image set, the mean pixel value has been calculated by averaging the ten mean values obtained from the same central part of each image over an area of 1280 pixels (H) × 512 pixels (V) (∼59 mm × 23 mm). The number of incoming photons was varied by means of the set of plexiglas attenuators and evaluated as described in §2.8.

2.6. Modulation transfer function (MTF)

The MTF is defined as the two-dimensional Fourier transform amplitude of the point spread function, which is the system response to a delta-shaped input signal; it is typically used to characterize the resolution properties of an imaging system in the spatial-frequency (u) domain. Since we wanted to access the one-dimensional MTF in both horizontal and vertical directions, we have chosen to calculate the MTF as the one-dimensional Fourier transform of the line spread function, as detailed later.

The crucial point in the calculation of the MTF is the fineness of the sampling of the signal: if the spatial frequencies are not sampled thinly enough to avoid aliasing, the system is no longer adequately described by the linear system model. If this is the case, the fundamental requirement of spatial invariance fails (Dobbins, 2000). Many different techniques have been developed to determine the MTF of a detection system. In the literature the MTF is experimentally determined by imaging a bar pattern test phantom, which gives the system response to a square-wave input signal (Johns & Cunningham, 1971; Borasi *et al.*, 2003). Alternatively, it is indirectly determined from the line spread function (LSF) or from the edge spread function (ESF), which are measured by imaging narrow slits (Fujita *et al.*, 1985) and opaque edges (Samei *et al.*, 1998), respectively. To overcome aliasing effects, refined methods foresee to slightly angle the slits (or the edge) in order to obtain more finely sampled LSF or ESF and the presampling MTF (Dobbins, 2000; Samei *et al.*, 1998; Greer & van Doorn, 2000).

In our determination of the MTF, we have chosen the edge method by using a 50 mm × 50 mm 0.3 mm-thick tungsten foil for all the energies. The ESF was measured in both the horizontal and vertical directions by acquiring an image of the edge phantom with a 2 μm scanning step (a). Each MTF is the average of the MTFs calculated by several determinations of the ESF (∼70 for the vertical direction and ∼20 for the horizontal). The horizontal ESFs were reconstructed by shifting each data row of a relative interval of 23 pixels (= horizontal pixel size/scanning step). From the ESF profiles, LSFs have been calculated by the finite-element difference method,

$$\mathrm{LSF}(x_j) = \mathrm{ESF}(x_{j+1}) - \mathrm{ESF}(x_j), \qquad (2)$$

where $\mathrm{LSF}(x_j)$ is the jth value of the LSF and $\mathrm{ESF}(x_j)$ and $\mathrm{ESF}(x_{j+1})$ are the adjacent values of the ESF.

As the differentiation process reduces the signal-to-noise ratio (SNR) (Cunningham & Fenster, 1987), the ESFs have been smoothed before LSF calculation by using the *Matlab* (The MathWorks, Natick, MA, USA) 'cubic smoothing spline' function.

Finally, the MTF has been determined as the modulus of the discrete Fourier transform of the LSF using a discrete spatial frequency interval (u) given by $1/Na$, where N is the number of sample points of the ESF. The presented MTF values have been normalized with respect to the MTF at zero frequency [MTF(0)].

2.7. Noise power spectrum (NPS)

The NPS represents a spectral decomposition of the variance of the image since it provides an estimation of the spatial frequency dependence of the pixel-to-pixel fluctuations originating both from the quantum noise of the X-ray beam and from any noise introduced in the electronic chain between

detector input and output (Williams *et al.*, 1999). In practice, it describes the different noise sources in a detection system and quantifies the effects of parameters, such as the exposure level and the energy, on the magnitude and texture of the noise. The two-dimensional digital NPS (Cunningham, 2000) has been determined as

$$\mathrm{NPS}(u_i, v_j) = \frac{\Delta x \Delta y}{N_x N_y}\left\langle \left|\mathrm{DFT2}(n_{ij})\right|^2 \right\rangle, \tag{3}$$

where x and y are the pixel spacing, N_x and N_y are the image dimensions in the x and y directions, n_{ij} is the two-dimensional noise image and DFT2 is the discrete two-dimensional Fourier transform.

Experimentally, ten 550 pixels × 2048 pixels flat-field images have been acquired for each evaluation of the NPS (at a given energy and exposure) by using the pipeline mode. Because the values along a column are affected mainly by temporal variations of the signal, a new 'noise image' was calculated from each of the ten original images by subtracting from each pixel the average pixel value of its relative column. With this operation, long-range (low-frequency) background trend and deterministic variability in the image owing to detector and/or beam spatial non-uniformity have been discarded; it has to be underlined that this procedure is not capable of removing the temporal fluctuations along the vertical direction.

In the analysis we considered a central portion of 1280 pixels (H) × 512 pixels (V) for each of the ten noise images. This area should be then subdivided into horizontally and vertically half-overlapped regions (IEC, 2002). Actually, there is always a trade-off when choosing the size and the number of these sub-regions. The larger the size of the sub-regions, the finer the frequency resolution of the resulting NPS, but also the fewer the number of regions available for averaging the NPS determinations (Dobbins *et al.*, 1995). In our case we used 27 sub-regions of 256 pixels × 256 pixels each.

In order to compare NPSs at different input fluxes the normalized noise power spectrum (NNPS) has been used,

$$\mathrm{NNPS}(u_i, v_j) = \mathrm{NPS}(u_i, v_j)\big/\langle P\rangle^2, \tag{4}$$

where $\langle P\rangle$ is the mean pixel values related to the sub-region over which the NPS was calculated. Each of the NNPSs presented in this paper is the average of the 270 normalized spectra obtained from the NPS calculated over the 270 sub-areas.

2.8. Calculation of the incoming photon flux

The incoming photon flux has been calculated using the germanium detector. Ten flat fields have been acquired for each combination of energy and attenuators used in the NPS calculation. The pedestal noise has been first subtracted from each flat field and then the average image counts were calculated. For these determinations a 173-pixel large ROI (60.55 mm) has been preliminarily selected on the germanium detector matching with the horizontal portion of the beam illuminating the ROI on the FReLoN camera. From the mean counts (expressed in bits) the number of the incoming photons per unit of area, time and storage-ring electron beam current has been calculated as (Corde, 2002)

$$\frac{\text{photons}}{\text{s m}^2\ \text{A}} = \frac{\text{bits } n_0\,[\text{photons/bit}]}{\tau\,[\text{s}]\ (p\,h)\,[\text{m}^2]\ I\,[\text{A}]\ G}, \tag{5}$$

where n_0 is the bit–photon conversion factor corresponding to the number of photons integrated by the germanium per bit at a given gain ($G = 1$ for all measurements); τ is the integration time, p is the horizontal pixel size, h is the measured X-ray beam height and I is the ring current (to which the photon flux is linearly proportional). The air-kerma (K) has been calculated as

$$K\,[\text{Gy}] = \text{bits } K_E\left[\frac{\text{Gy}}{\text{m bit}}\right]\frac{\tau_{\text{Fr}}\,[\text{s}]\ \text{pxla}_{\text{Fr}}\,[\text{m}^2]\ I_{\text{Fr}}\,[\text{A}]}{\tau_{\text{Ge}}\,[\text{s}]\ h_{\text{Ge}}\,[\text{m}]\ I_{\text{Ge}}\,[\text{A}]\ G}\,\frac{\mu_{\text{air}}}{\mu_{\text{water}}}, \tag{6}$$

where K_E is a factor including all the energy-dependent terms like the energy itself, the water mass attenuation coefficient and the horizontal pixel size (p). The subscripts indicate the detector used, and pxla is the FReLoN camera pixel area, while μ_{air} and μ_{water} are the air and water mass attenuation coefficients, respectively.

2.9. Detective quantum efficiency (DQE)

Once the MTF, the NPS and the input SNR of the X-ray beam used to measure the NPS are known, the DQE can be calculated assuming a linear shift-invariant detection system. The DQE is a paradigmatic performance parameter of digital X-ray detectors since it is a frequency-dependent measure of the efficiency of the system in reproducing the information contained in the incident X-ray signal.

In other words, this parameter expresses the degradation in the SNR introduced by the processes of detection and conversion of the X-ray signal and it is defined as the square of the ratio of the SNR at the detector output to that at its input. Experimentally, the calculation of the frequency-dependent DQE of a linear system can be deduced from the measured presampling MTF and NNPS (Cunningham, 2000),

$$\mathrm{DQE}(u) = \frac{\mathrm{MTF}^2(u)}{\mathrm{NNPS}(u)}\frac{1}{q}, \tag{7}$$

where q is the mean number of incident quanta per unit of area and corresponds to the input-squared SNR. The DQEs of the system have been computed for one-dimensional spatial frequencies in the horizontal and vertical directions by using the one-dimensional NNPS projections.

3. Results

The energy dependence of the detector performances has been investigated by measuring MTF, NNPS and DQE for several energies and two different fluorescent screen thicknesses as reported in Table 1.

Table 1
Energies considered in this work for the two fluorescent screens.

Screen (μm)	Energy (keV)
40	20, 25, 33
100	25, 33, 51.5

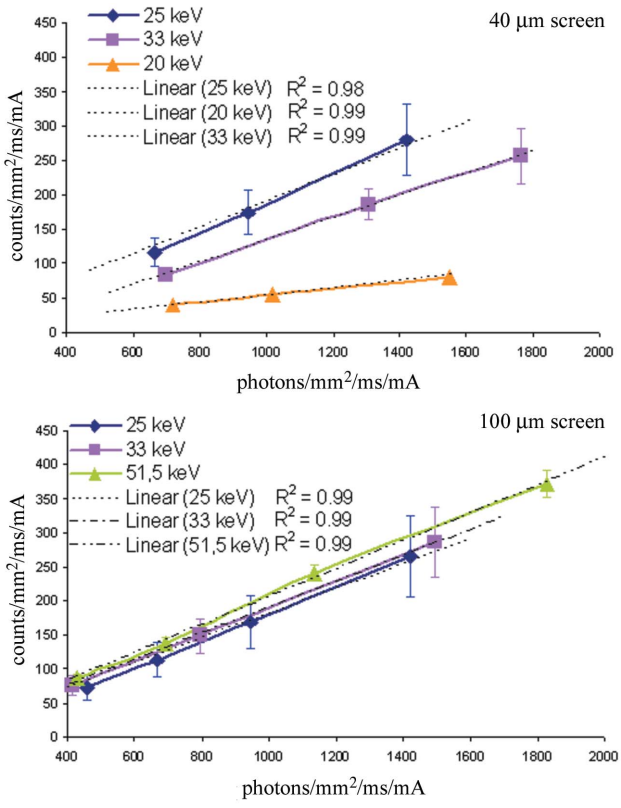

Figure 5
Large-area transfer characteristics for the two screens at 20, 25, 33 and 51.5 keV. Counts of the FReLoN *versus* the calculated number of photons are reported, normalized per unit of area, time and storage ring electron beam current.

Table 2
Spatial frequencies (mm^{-1}) corresponding to 50%, 10% and 5% of the MTF in the horizontal (H) and vertical (V) directions.

Each value is affected by an error estimated in 0.2 mm^{-1}.

Screen thickness (μm)	Energy (keV)	50%		10%		5%	
		H	V	H	V	H	V
40	20	3.7	4.0	8.2	9.0	10.0	10.7
	25	3.9	4.1	8.5	9.0	10.1	10.6
	33	4.1	4.0	8.5	9.2	9.9	10.6
100	25	3.7	3.6	7.8	8.0	9.6	10.2
	33	3.7	3.8	7.8	8.6	9.8	10.1
	51.5	3.5	3.4	7.6	7.8	8.9	9.5

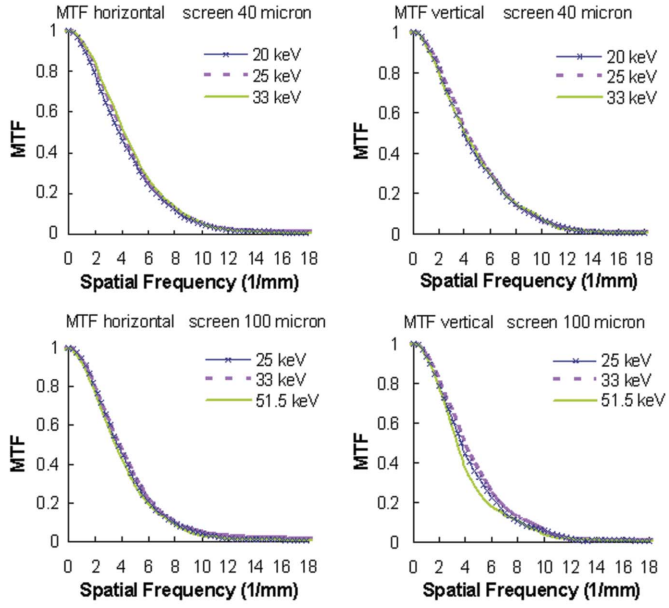

Figure 6
MTF along the horizontal and vertical directions for the 40 and 100 μm-thick screens.

In order to justify the use of the theory for linear systems, the linearity of the system response has been verified over the exposure range considered in the rest of the evaluation. The results are shown in Fig. 5 where the large-area transfer characteristic curves of the FReLoN camera are presented for the different energies and the two screens. In all of the cases (except the 40 μm screen at 25 keV, where $R^2 = 0.98$) the linear fit of the experimental data has an *R*-squared coefficient of 0.99.

Fig. 6 illustrates the presampling MTF measured in both directions. For a given fluorescent screen the MTF slightly changes with the energy but the MTF curves are almost overlapping. In Table 2 the spatial frequencies corresponding to 50%, 10% and 5% of the MTF are reported. In most of the cases the MTF values in the vertical direction are slightly higher than in the horizontal. Fig. 7 shows the MTF curves at 25 and 33 keV for the two fluorescent screens. As expected, the MTF worsens when the thickest screen is used. Fig. 8 shows how the MTF is influenced by the acquisition and readout modes (concatenate and the pipeline modes at binning 1, 4 and 8).

Figs. 9 and 10 report the one-dimensional cuts of the NNPS along the two directions after having averaged a few rows/columns on both sides of the axes, and having omitted the axes themselves. As expected, owing to the weaker contribution of the stochastic (quantum) noise the normalized noise power decreases when the exposure level increases. For all of the energy-exposure cases, the NNPS projections show different behaviors: in the horizontal direction the NNPS systematically decreases as the spatial frequency increases, while in the vertical (temporal) direction the NNPS has a flat profile with, in many cases, some larger fluctuations at high frequencies where the quantum noise prevails.

Figs. 11 and 12 illustrate the DQE for the same cases considered in the NNPS analysis. For an ideal linear detector, characterized by the absence of any additive (or multiplicative) system noise, the DQE does not depend on *q* (Cunningham, 2000). This kind of behavior is also shown in the results of the present study for the investigated *q* range. For a given fluorescent screen and at a fixed energy, the DQEs

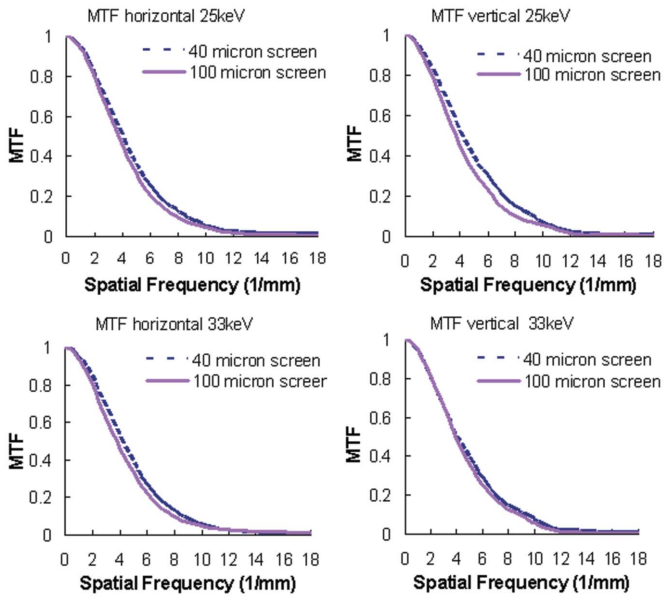

Figure 7
Comparison of the horizontal and vertical MTFs at 25 and 33 keV for the two fluorescent screens.

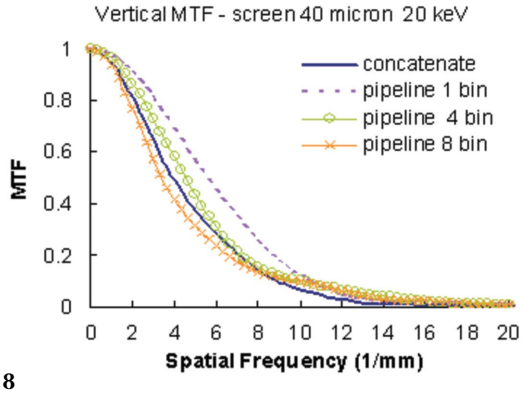

Figure 8
Measured MTFs in 'concatenate' and 'pipeline' acquisition modes at 20 keV for the 40 µm screen.

determined at different exposures overlap over almost the entire frequency interval considered here. Deviations from the ideal case concern the low frequency values that are largely affected by the NNPS artefacts, and the DQE in the vertical direction, because of temporal fluctuations of the X-ray beam. Moreover, the vertical DQE is slightly smaller than the horizontal, because the vertical NNPS is larger than the horizontal.

4. Discussion

In this paper we have investigated the resolution (presampling MTF), the noise (NNPS) and the signal-to-noise ratio (DQE) properties of the FReLoN camera, an indirect conversion digital radiographic system developed at the ESRF for preclinical medical imaging applications.

The presampling MTF was determined by using an edge analysis, since several studies have demonstrated that, in comparison with the slit technique, it is a simple and accurate method for measuring the low- and mid-frequency response of a system and it provides adequate results also at the high-frequency domain (Samei *et al.*, 1998; Cunningham & Fenster, 1987).

The comparison of the presampling MTFs for the two fluorescent screens at the same energy shows that by increasing the screen thickness the spatial resolution worsens because of the increased scattering of the visible light.

As reported in the literature (Borasi *et al.*, 2003), increasing the energy (for a given fluorescent screen thickness) should result in a spatial resolution improvement since the mean photon–gadox screen interaction point is deeper, and therefore light scattering inside the fluorescent screen is limited. This behavior is theoretically true in the X-ray energy range where the linear attenuation coefficient monotonically decreases with the energy. Besides, in an energy interval containing a fluorescent screen absorption edge, an opposite trend should be observed among X-ray energies ahead of and after the edge. The latter behavior was experimentally verified here in terms of MTF worsening at 51.5 keV (just 0.5 keV higher than the gadolinium *K*-edge) with respect to the 33 keV MTF. Experimentally, the horizontal MTF at 10% is 7.8 at 33 keV and 7.6 at 51.5 keV, while the vertical MTF at 10% is 8.6 at 33 keV and 7.8 at 51.5 keV for the 100 µm screen (Table 2).

The slight difference between the MTFs in the two directions (higher values in the vertical direction) may be related to the readout electronics bandwidth; in fact, it can be attributed to a small residual charge left on the register pixel when the signal moves horizontally during the readout.

Not surprisingly, a comparison of the MTF curves obtained by different detector acquisition readout modes (Fig. 8) reveals that the best spatial resolution is achieved when operating without binning.

Also as expected, the NNPS is exposure dependent (higher at lower exposures); this behavior is related to the Poisson distribution of the quantum noise component of an X-ray image. In addition, in all of the considered exposure-energy cases, the NNPS presents significant higher values near the zero frequency, where the deterministic noise component prevails. The low-frequency effects are less evident at low exposures as they are masked by the stochastic contributions. The trend of the NNPS along the horizontal and vertical direction is different, as shown in Figs. 9 and 10. In the horizontal direction the NNPS constantly decreases as it moves towards the high-frequency domain. This behavior is typical of detectors based on indirect conversion and is determined by the spatial correlation between adjacent pixels that read the same signal because of the light scattering of the screen (Samei & Flynn, 2003). On the contrary, the vertical NNPS is almost flat. Along this direction the noise spectrum depends mainly on the time variations of the X-ray beam and therefore at high frequencies the graphs show an increase in the NNPS values. At low exposures this increase is less evident because the stochastic (quantum) noise component dominates.

The high contribution of the deterministic component of the NNPS at high exposures affects the DQE shape in the vicinity

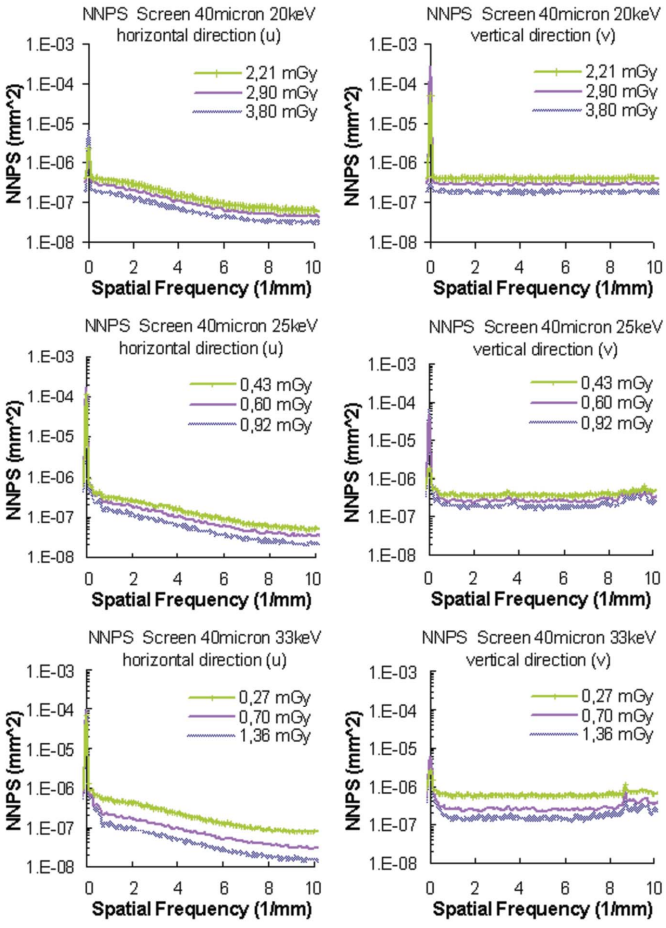

Figure 9
NNPS in the horizontal and vertical directions for the 40 µm-thick screen at 20, 25 and 33 keV.

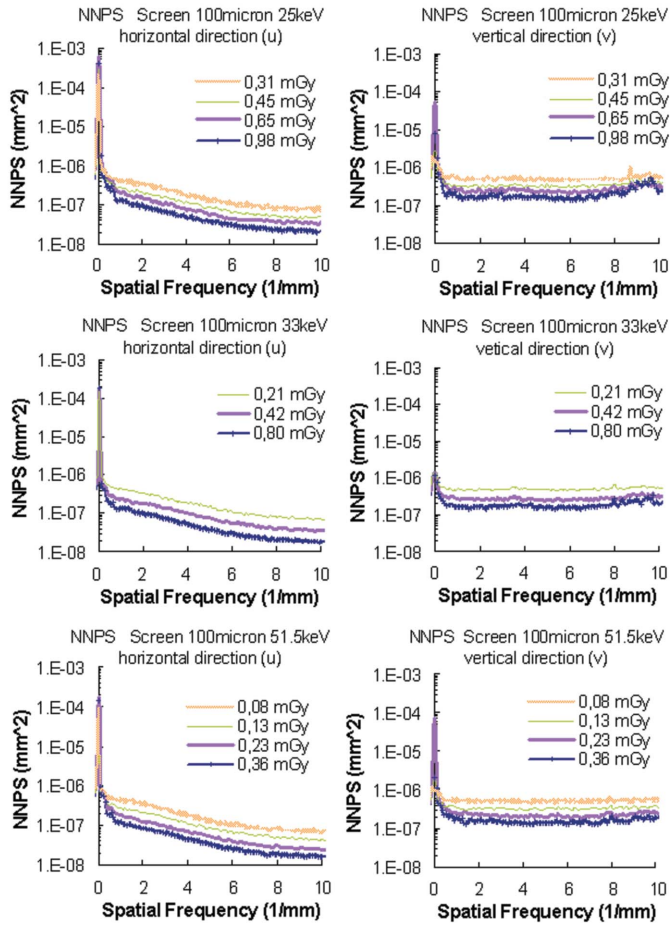

Figure 10
NNPS in the horizontal and vertical directions for the 100 µm-thick screen at 25, 33 and 51.5 keV.

of the zero-frequency. For the 100 µm screen the DQEs at 51.5 keV (just above the *K*-edge of the gadolinium-based fluorescent screen) present values similar or even higher than those at 33 keV. This result is explained by the abrupt increase in the photon interaction cross section at the *K*-edge of the element, which therefore increases the light yield production of the screen. As shown, the DQE values for the 40 µm screen are of the same order as those for the 100 µm since the 40 µm phosphor screen is optimized for spatial resolution and not for DQE.

Several factors contribute to limiting the DQE. The phosphor screen conversion yield certainly plays an important role; thicker screens would be more efficient in particular at high energies, but the detriment of the spatial resolution would not be acceptable for applications like mammography (Bravin *et al.*, 2003). A second important role is played by the low efficiency of the CCD [about 25% (Atmel, 2002)] which registers only a fraction of the visible photons emitted by the screen. Of importance is also the fact that the choice we made in the detector construction, *i.e.* to permit an easy change of the fluorescent screen, prevents the optimization of the optical contact between the fluorescent screen itself and the taper (the present layout makes it difficult to avoid air gaps in between).

Higher DQE values would be of particular importance for *in vivo* imaging when the dose delivered to the sample has to be kept as low as possible. In the new version of this detector prototype, presently under development, we will work to reduce efficiency losses by using a more efficient CCD and by improving the screen–taper contact.

5. Comparison of the taper optics FReLoN camera performances with X-rays detectors in the literature

In order to better appreciate the characteristics and performances of the taper optics FReLoN camera they are compared (Table 3) with X-ray imaging detectors presented in the literature, by focusing our attention on the field of view, pixel size, MTF, DQE and readout speed. For the FReLoN camera we have chosen to report results for the 100 µm-thick screen only.

It should be noted, however, that care should be taken when interpreting such a table. The different experimental conditions, under which each of these detectors has been characterized (reported in the table when available), make the comparison difficult and often unfair; in fact, performances strongly depend on the energy used for the characterization and on the applied binning. In addition, specific detector

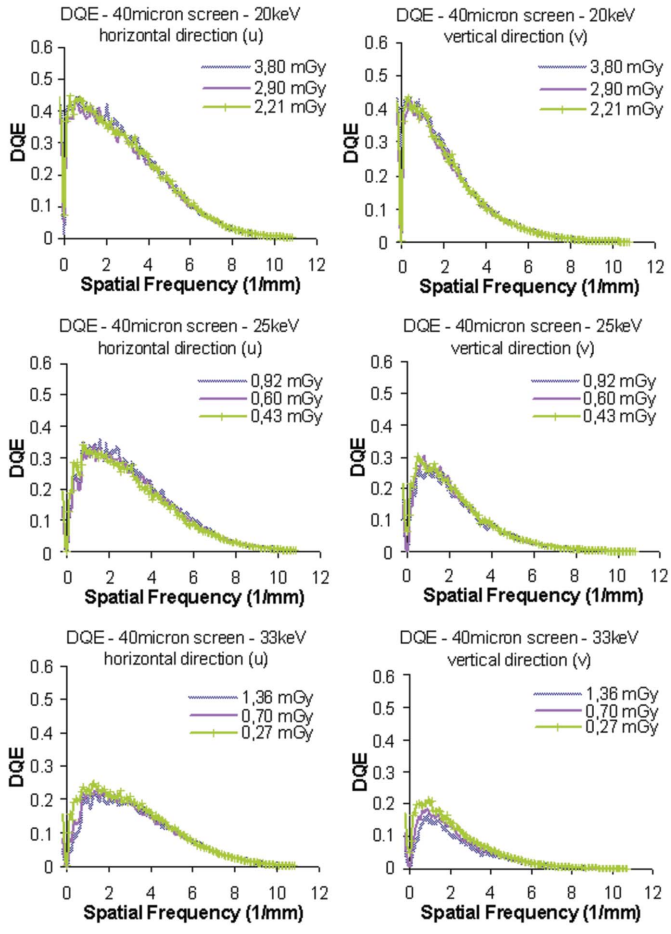

Figure 11
DQE in the horizontal and vertical directions for the 40 μm-thick screen at 20, 25 and 33 keV.

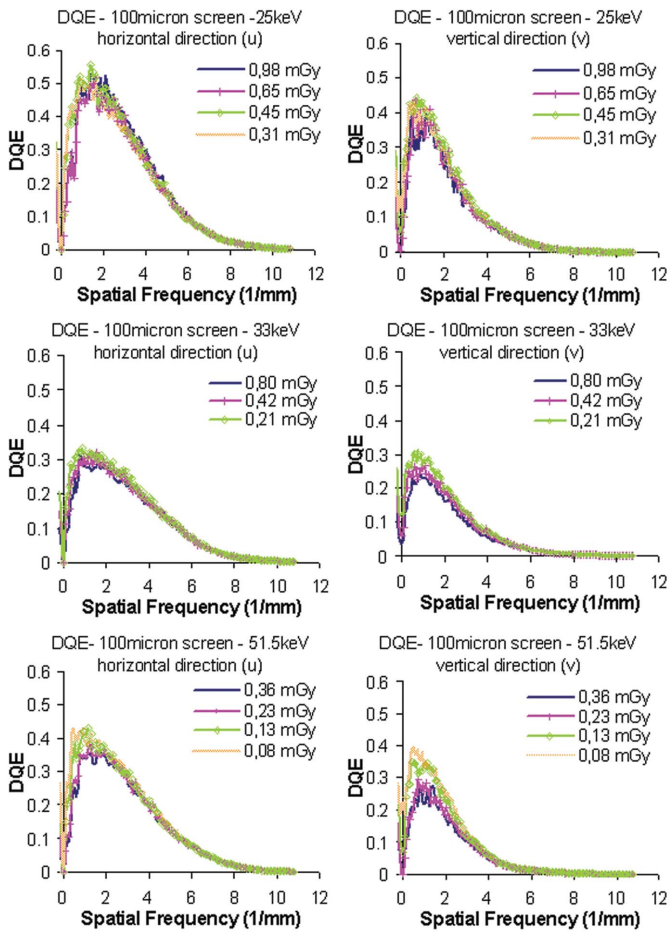

Figure 12
DQE in the horizontal and vertical directions for the 100 μm-thick screen at 25, 33 and 51.5 keV.

layouts (like the availability of different readout modes for the FReLoN camera) are not mentioned in the literature on other detectors. Such features may play a critical role in the detector choice. Despite these limitations, data reported in Table 3 indicate where the FReLoN is positioned with respect to synchrotron radiation medical imaging needs.

The most commonly used devices for high-resolution imaging are CCDs and FPs. CCDs are typically characterized by low noise, a small pixel size (typically tens of micrometers or less) and a large pixel number (up to $\sim 3.0 \times 10^7$ so far); on the other hand, CCDs are easily damaged by X-rays and their readout is limited by the charge transporting method. This is why CCD-based detectors are generally combined with tapered optical fibers and/or with indirect lens-coupling or intensifier (Yagi *et al.*, 2004; Vedantham *et al.*, 2000).

Amorphous silicon detectors (for instance #9 in Table 3) are another important category of solid-state detectors; they are built on a photodiode array with an active TFT (thin-film transistor) matrix readout which can be quite big (#9, #10). Their sensitivity to X-rays is achieved by using amorphous selenium as the converting medium (X-rays to electrons) or by coupling them with a scintillator (X-rays to visible light conversion). In general, even if this kind of detector can achieve high efficiency, it has severe limitations in terms of spatial resolution (pixel size >100 μm) and noise. A good compromise is offered by the amorphous-Se direct detector Thermotrex (#11); it presents a pixel size of 66 μm and good spatial resolution and DQE compared with other detectors in the same category (#9, #10). A point which remains to be verified is the readout speed that is not reported in the literature. Another example in the same category is the amorphous-Si flat panel coupled to thallium-doped caesium iodide (CsI:Tl) (GE, #9) that presents a readout speed faster than the FReLoN, but a much worse spatial resolution.

An alternative is the CMOS (complementary metal-oxide semiconductor) FP. Hamamatsu Photonics (#8 in Table 3) has an active area larger than the FReLoN and the same pixel size. Moreover, the direct deposition of the scintillator on the taper allows the spatial resolution of the CMOS FP to be increased, resulting in a very competitive device. A weak aspect is the low readout speed, which is half of the FReLoN readout speed.

Other CCD-based detectors reported in the literature are presented in Table 3 (lines 1–7). Among them, the FReLoN has one of the largest areas and fastest readout.

Very fast readout (291 frames s^{-1}) is achieved by the C7770 Hamamatsu Photonics KK detector (#5) which is based on

Table 3
Selected characteristics of the FReLoN camera compared with some other detectors used in X-ray imaging.

Values reported here have been extracted from graphs shown in the reference papers (column 9). The energy refers to the X-ray beam used for the detector characterization; in the absence of notes, synchrotron radiation monochromatic beams have been used.

Detector	Dimensions (mm)	Number of pixels	Pixel size (μm)	10% MTF (mm^{-1})	DQE at 0 mm^{-1}	X-ray beam energy (keV)	Readout speed (frames s^{-1})	Reference
1. FReLoN coupled to 100 μm Gadox screen†	94 × 94	2048 × 2048	46 × 46	8.0	∼42%	25	4.2	This work
				8.6	∼30%	33		
				7.8	∼35%	51.5		
2. Dalsa-Medoptics CCD with a 3:1 fiber taper and GOS screen	69 × 69	1024 × 1024	67.55 × 67.55	∼8.0	∼30%	∼21‡	–	(Goertzen *et al.*, 2004)
3. Dalsa-Medoptics CCD with a 2:1 fiber taper and GOS screen	49 × 49	1024 × 1024	48.23 × 48.23	∼8.0	∼24%	∼21‡	–	(Goertzen *et al.*, 2004)
4. Dalsa-Medoptics CCD with a 2:1 fiber taper and CsI:Tl screen	49 × 49	1024 × 1024	48.23 × 48.23	∼9.3	∼40%	∼21‡	–	(Goertzen *et al.*, 2004)
5. C7770 Hamamatsu Photonics KK + prism + 3 CCDs with intensifier	6.5 × 4.9	656 × 494	9.9 × 9.9	–	–	–	291	(Yagi *et al.*, 2004)
6. Philips FTF7040 CCD with Gadox screen	49 × 86	4096 × 7168	12 × 12	∼16 (2 × 2 binning)	∼65% (2 × 2 binning)	12§	0.14	(Phillips *et al.*, 2002)
7. CCD Senovision, GE Medical Systems	61 × 61	4096 × 4097	15 × 15 30 × 30 (binned)	∼10	∼40%–28% (depending on exposure)	28 kV Mo filter	–	(Vedantham *et al.*, 2000)
8. CMOS flat-panel imager from Hamamatsu Photonics (C7942)	120 × 120	2240 × 2368	50 × 50	∼6.5 ∼10.0¶	–	20	2	(Yagi *et al.*, 2004)
9. Amorphous-Si flat panel coupled to CsI:Tl scintillator (Revolution XQ/i, GE Medical Systems)	410 × 410	2048 × 2048	200 × 200	∼1.6 (at 50% MTF)	∼66%	∼50‡	8	(Granfors & Aufrichtig, 2000)
10. Amorphous-Se flat panel, Direct Radiography (Hologic) DR-1000 (DRC)	350 × 350	2560 × 3072	139 × 139	∼6.4	∼38%	∼50‡	–	(Samei & Flynn, 2003)
11. Amorphous-Se Thermotrex	67.5 × 54.9	1024 × 832	66 × 66	∼5.5 (at 50% MTF)	∼55%	∼21‡	–	(Goertzen *et al.*, 2004)
12. Si microstrip detector	50 × 1	512 × 3	200 × 300	∼6	–	20	–	(Olivo *et al.*, 2003)

† MTF and DQE (columns 5 and 6, respectively) correspond to results calculated in the vertical direction. ‡ Mean energy in keV has been estimated from the half-value layer values given in the paper. § Mean energy declared in the paper. ¶ Modified version of the CMOS flat-panel imager from Hamamatsu Photonics (C7942) obtained by direct deposition of the scintillator (CsI:Tl) on the photodiode array.

three CCDs alternatively read and coupled to an X-ray image intensifier; the pixel size is only 9.9 μm but the detector dimensions are too small for *in vivo* medical imaging (6.5 mm × 4.9 mm).

A relatively large active area (49 mm × 86 mm) and small pixel size (12 μm) characterize the Philips FTF7040 CCD (#6); it also presents good values for both MTF and DQE. The readout speed is nevertheless quite limited for medical imaging (0.14 frames s^{-1}).

Goertzen *et al.* (2004) reported the evaluations of two Dalsa-Medoptics CCDs: the first one (CCD1) (#2) is coupled to a fiberoptic taper with a 3:1 demagnification and gadolinium oxysulphide (GOS) phosphor screen converter; the second CCD (CCD2) is coupled to a fiberoptic taper with a 2:1 demagnification and to a changeable scintillator that can be either a GOS (#3) or a CsI:Tl (#4) screen. For the CCD2, the CsI:Tl screen results in almost twice the DQE with respect to the GOS screen (0.4 *versus* 0.24 at 0 mm^{-1}); CCD2 shows MTF values almost identical to CCD1 when the GOS screen is used.

The pixel size for both these CCD-based devices is comparable with that of the FReLoN camera; nevertheless, since the number of pixels is limited to 1024 × 1024, the resulting detector area is smaller than the FReLoN. In addition, considering that the MTF and DQE values of these CCDs have been measured with a 21 keV-equivalent X-ray beam, it is possible to conclude that the FReLoN camera offers similar or even better performances (see also Table 2 and Fig. 11 for data at 20 keV) both in terms of spatial resolution and efficiency in a rather wide energy range (the readout speed values are not available).

Among the direct conversion systems, an important category is represented by the silicon detectors. An interesting example is the three-layer edge-on microstrip detector (Olivo *et al.*, 2003). It has an active area of 50 mm × 1 mm, matching well with the synchrotron radiation laminar shape, and it is associated with low-noise single-photon-counting electronics (#12). A limitation of such detectors is in the relatively large pixel size of 200 μm × 300 μm (horizontal × vertical).

This comparison shows that the performances of the FReLoN camera in its present version position it very well in the X-ray imaging detector world. Not one of the detectors presented exceeds the FReLoN camera in all parameters simultaneously; this is the outcome of the compromise made in the camera layout to fit with the synchrotron radiation medical imaging needs. In addition, the camera offers the advantage of data acquisition modes specifically tailored to a synchrotron radiation laminar beam. Very likely its performances will be improved even further, in terms of efficiency, in the newest version currently under development.

The authors thank C. Nemoz, T. Brochard, G. Berruyer and M. Renier for their invaluable support in this experimental work, and C. Wong for the manuscript revision.

References

Adam, J., Nemoz, C., Bravin, A., Fiedler, S., Bayat, S., Monfraix, S., Berruyer, G., Charvet, A., Le Bas, J. F., Elleaume, H. & Esteve, F. (2005). *J. Cereb. Blood Flow Metab.* **25**, 145–153.

Arfelli, F., Bonvicini, V., Bravin, A., Cantatore, G., Castelli, E., Dalla Palma, L., Di Michiel, M., Fabrizioli, M., Longo, R., Menk, R.-H., Olivo, A., Pani, S., Pontoni, D., Poropat, P., Prest, M., Rashevsky, A., Ratti, M., Rigon, L., Tromba, G., Vacchi, A., Vallazza, E. & Zanconati, F. (2000). *Radiology*, **215**, 286–293.

Atmel (2002). Full field CCD image sensor 2048 × 2048 pixels (TH7899M), Rev. 2201A-IMAGE-02/02 Datasheets. Atmel, San Jose, CA, USA.

Bertrand, B., Estève, F., Elleaume, H., Némoz, C., Fiedler, S., Bravin, A., Berruyer, G., Brochard, T., Renier, M., Machecourt, J., Thomlinson, W. & Le Bas, J. F. (2005). *Eur. Heart J.* **26**, 1284–1291.

Borasi, G., Nitrosi, A., Ferrari, P. & Tassoni, D. (2003). *Med. Phys.* **30**, 1719–1731.

Bravin, A., Fiedler, S., Coan, P., Labiche, J.-C., Ponchut, C., Peterzol, A. & Thomlinson, W. (2003). *Nucl. Instrum. Methods*, A**510**, 35–40.

Coan, P., Pagot, E., Fiedler, S., Cloetens, P., Baruchel, J. & Bravin, A. (2005). *J. Synchrotron Rad.* **12**, 241–245.

Corde, S. (2002). PhD thesis, Université J. Fourier, Grenoble, France.

Cunningham, I. (2000). *Handbook of Medical Imaging*, Vol. 1, edited by R. L. Van Metter, J. Beutel and H. Kundel H, ch. 2, pp. 79–159. Washington: SPIE.

Cunningham, I. & Fenster, A. (1987). *Med. Phys.* **14**, 533–537.

Dobbins, J. I. (2000). *Handbook of Medical Imaging*, Vol. 1, edited by R. L. Van Metter, J. Beutel and H. Kundel H, ch. 3, pp. 161–221. Washington: SPIE.

Dobbins, J. I., Ergun, D., Rutz, L., Hinshaw, D., Blume, H. & Clark, D. (1995). *Med. Phys.* **22**, 1581–1593.

Elleaume, H., Charvet, A.-M., Berkvens, P., Berruyer, G., Brochard, T., Dabin, Y., Dominguez, M., Draperi, A., Fiedler, S., Goujon, G., Le Duc, G., Mattenet, M., Nemoz, C., Perez, M., Renier, M., Schulze, C., Spanne, P., Suortti, P., Thomlinson, W., Esteve, F., Bertrand, B. & Le Bas, J.-F. (1999). *Nucl. Instrum. Methods*, A**428**, 513–527.

Follet, H., Bruyere-Garnier, K., Peyrin, F., Roux, J., Arlot, M., Burt-Pichat, B., Rumelhart, C. & Meunier, P. (2005). *Bone*, **36**, 340–351.

Fujita, H., Doi, K. & Giger, M. (1985). *Med. Phys.* **12**, 713–720.

Goertzen, A. L., Nagarkar, V., Street, R. A., Paulus, M. J., Boone, J. M. & Cherry, S. R. (2004). *Phys Med. Biol.* **49**, 5251–5265.

Granfors, P. R. & Aufrichtig, R. (2000). *Med. Phys.* **27**, 1324–1331.

Greer, P. & van Doorn, T. (2000). *Med. Phys.* **27**, 2048–2059.

IEC (2002). International Electrotechnical Commission, San Diego, USA.

Johns, H. & Cunningham, J. (1971). *The Physics of Radiology.* Springfield, IL: Thomas.

Monfraix, S., Bayat, S., Porra, L., Berruyer, G., Nemoz, C., Thomlinson, W., Suortti, P. & Sovijarvi, A. R. A. (2005). *Phys. Med. Biol.* **50**, 1–11.

Olivo, A., Pani, S., Dreossi, D., Montanari, F., Bergamaschi, A., Vallazza, E., Arfelli, F., Longo, R., Rigon, L. & Castelli, E. (2003). *Rev. Sci. Instrum.* **74**, 3460–3465.

Pagot, E., Fiedler, S., Cloetens, P., Bravin, A., Coan, P., Fezzaa, K., Baruchel, J. & Härtwig, J. (2005). *Phys Med. Biol.* **50**, 709–724.

Peterzol, A., Bravin, A., Coan, P. & Elleaume, H. (2003). *Nucl. Instrum. Methods*, A**510**, 45–50.

Phillips, W. C., Stewart, A., Stanton, M., Naday, I. & Ingersoll, C. (2002). *J. Synchrotron Rad.* **9**, 36–43.

Samei, E. (2003). *Med. Phys.* **30**, 1747–1757.

Samei, E. & Flynn, M. (2003). *Med. Phys.* **30**, 608–622.

Samei, E., Flynn, M. & Reiman, D. (1998). *Med. Phys.* **25**, 102–113.

Suortti, P., Fiedler, S., Bravin, A., Brochard, T., Mattenet, M., Renier, M., Spanne, P., Thomlinson, W., Charvet, A.-M., Elleaume, H., Schulze-Briese, C. & Thompson, A.-C. (2000). *J. Synchrotron Rad.* **7**, 340–347.

Suortti, P. & Thomlinson, W. (2003). *Phys. Med. Biol.* **48**, R1–R35.

Tafforeau, P., Boistel, R., Boller, E., Bravin, A., Brunet, M., Chaimanee, Y., Cloetens, P., Feist, M., Hoszowska, J., Jaeger, J.-J., Kay, R. F., Lazzari, V., Marivaux, L., Nel, A., Nemoz, C., Thibault, X., Vignaud, P. & Zabler, S. (2006). *Appl. Phys. A*, doi:10.1007/s00339-006-3507-2.

Vedantham, S., Karellas, A., Suryanarayanan, S., Levis, I., Sayag, M., Kleehammer, R., Heidsieck, R. & D'Orsi, C. (2000). *Med. Phys.* **27**, 1832–1840.

Williams, M., Mangiafico, P. & Simoni, P. (1999). *Med. Phys.* **26**, 1279–1293.

Yagi, N., Inoue, K. & Oka, T. (2004). *J. Synchrotron Rad.* **11**, 456–461.

Yagi, N., Yamamoto, M., Uesugi, K. & Inoue, K. (2004). *J. Synchrotron Rad.* **11**, 347–352.